Electrical detection of domain evolution in magnetic Weyl semimetal $Co_3Sn_2S_2$ submicrometer-wide wire devices

Junichi Shiogai [1,2,*], Junya Ikeda,[1] Kohei Fujiwara [1], Takeshi Seki [1], Koki Takanashi [1,3,4] and Atsushi Tsukazaki [1,3]

[1]*Institute for Materials Research, Tohoku University, Sendai 980-8577, Japan*
[2]*Department of Physics, Osaka University, Toyonaka 560-0043, Japan*
[3]*Center for Science and Innovation in Spintronics, Core Research Cluster, Tohoku University, Sendai 980-8577, Japan*
[4]*Advanced Science Research Center, Japan Atomic Energy Agency, Tokai 319-1195, Japan*

Microscopic understanding of magnetization switching via domain nucleation and/or domain-wall propagation is fundamental knowledge for developing magnetic and spintronic devices. Here, we explore the underlying mechanism of the large coercivity of the magnetic Weyl semimetal $Co_3Sn_2S_2$ thin films, which is roughly ten times larger than that of $Co_3Sn_2S_2$ bulk single crystal, by measuring Hall resistance in constricted wire devices. The discretized steplike variations appear in the hysteresis loops of the Hall resistance in 0.6 μm wide and narrower devices, indicating that the size of the reversed magnetic domain is comparable to the active area of the Hall devices. By counting the number of discrete features, the average diameter of the reversed magnetic domain is estimated to be 80 nm. Individually, the diameter of the reversed domain nucleus is evaluated to be roughly 2 nm. Considering the difference in the diameters of the reversed magnetic domain and the reversed domain nucleus, we ascribed the large coercivity of the $Co_3Sn_2S_2$ thin films to a large nucleation field owing to the uniform crystallinity within grains and strong domain-wall pinning at grain boundaries specific to the thin films. With the large nucleation field in the films, an engineering of the domain-wall pinning sites is a promising approach to control the nucleation, manipulation, and detection of the single domain wall in $Co_3Sn_2S_2$ thin-film devices.

I. INTRODUCTION

Magnetic Weyl semimetal (mWSM) is a new class of topological materials exhibiting exotic magnetic responses originating from a pair of Weyl points in the electronic structure [1–3]. Thanks to the contribution of Berry curvature at the singular points, various giant magnetic responses emerge such as a large anomalous Hall effect (AHE) [4–6], anomalous Nernst effect (ANE) [7–14], and enhanced magneto-optical responses [15,16]. At the boundary of magnetic domains of mWSMs, chiral features of the two Weyl points are connected across the domain wall (DW). In such a situation, the emergence of a one-dimensional chiral channel at the DW [17], anomalous magnetotransport with DW dynamics [18–20], and efficient current-induced DW displacement [21] have been theoretically proposed. For achieving such exotic physical phenomena at the DW experimentally, it is critically important to obtain fundamental knowledge on the magnetization switching and the subsequent magnetic domain formation with DW motion in mWSM thin films by fabricating a microscopic device and evaluating the magnetization switching process in detail.

A cobalt shandite-type compound $Co_3Sn_2S_2$ [22] with a two-dimensional kagome lattice of Co in its crystal structure [Fig. 1(a)] has been intensively studied owing to the

half-metallic electronic structure [23] and the large perpendicular magnetic anisotropy (PMA) with the coercivity $\mu_0 H_c$ of roughly 0.3 T and the very large magnetic anisotropy field $\mu_0 H_A$ of roughly 20 T at 2 K, where μ_0 is permittivity in vacuum [5,24]. $Co_3Sn_2S_2$ has gained a renewed interest after the discovery of the giant intrinsic AHE and ANE in the bulk single crystals [4,5,10,12] that are the characteristics of mWSM [25,26]. Magnetic domain and spin structure of the $Co_3Sn_2S_2$ bulk single crystals have been fairly studied using spatially resolved *in situ* measurements [27,28]. Under the zero-field cooling across the Curie temperature T_C, the maze pattern of magnetic domains with the linear-type DW was observed resulting from the very large PMA [28]. In the magnetic field sweep below T_C, the reversed magnetic domain is formed and its size is estimated to be of the order of a few to hundreds of micrometers [28,29]. The magnetization switching is driven by the formation of the reversed magnetic domain and DW propagation [29], which can explain the much smaller $\mu_0 H_c$ of 0.3 T at $T = 2$ K than $\mu_0 H_A$ of 20 T in bulk single crystals [5,6]. Despite the well-understood magnetization switching mechanism in the bulk crystals, that of the $Co_3Sn_2S_2$ thin film remains elusive. Recent progress of the synthesis of the $Co_3Sn_2S_2$ thin films [30,31] has made it possible to investigate the electrical transport and magnetic properties of the thin films [32–34]. It has been revealed that the three characteristic properties of a large AHE, PMA character, and large H_A of about 20 T are maintained in the thin-film form [30,34]. The distinct feature of the films is the large H_c on the order of a few
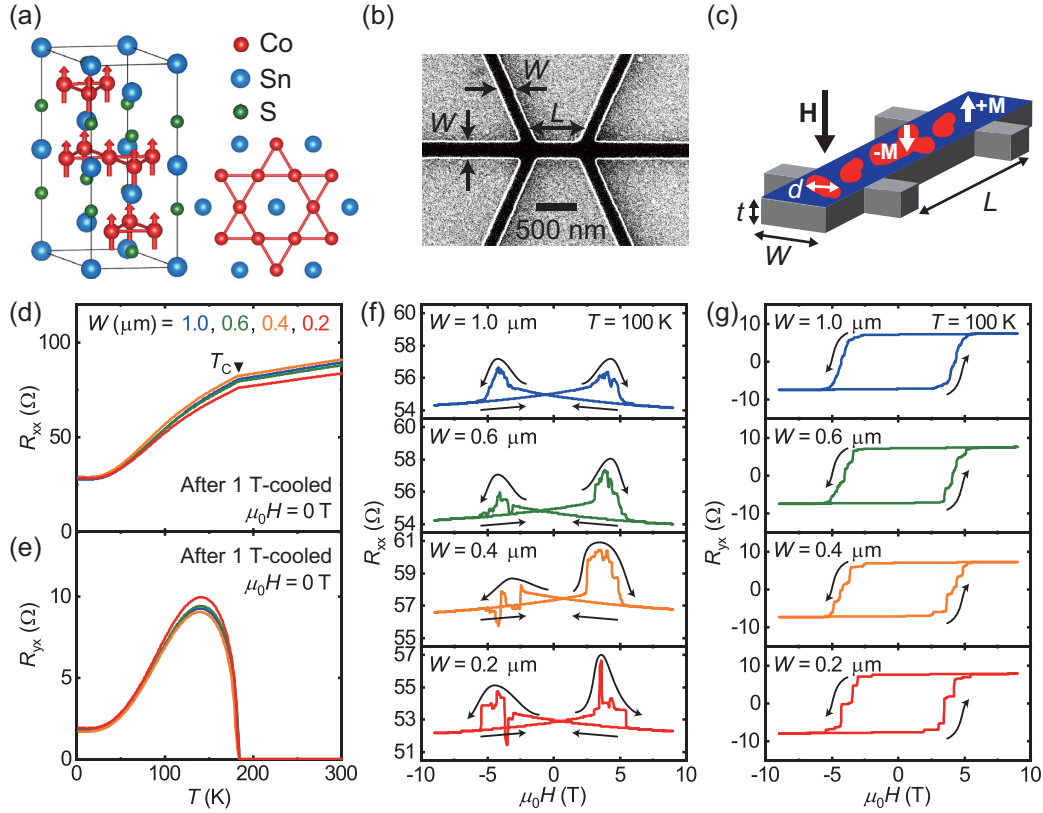
*junichi.shiogai.sci@osaka-u.ac.jp

FIG. 1. (a) Crystal structure of $Co_3Sn_2S_2$. The crystal structure was visualized using VESTA [58] (b) A scanning electron micrograph of an electron-beam resist (dark region) patterned on an SiO_x-capped $Co_3Sn_2S_2$ thin film taken before the Ar ion milling. (c) Schematic of a $Co_3Sn_2S_2$ Hall-bar device. A magnetic field H was applied perpendicular to the film plane. The separation of voltage probes is L and the channel width is W. A diameter of the reversed magnetic domain is defined as d. (d), (e) Temperature dependences of (d) sheet resistance (R_{xx}) and (e) Hall resistance (R_{yx}) measured at zero magnetic field after field cooling at $\mu_0 H = 1$ T. (f), (g) $\mu_0 H$ dependences of (f) R_{xx} and (g) R_{yx} measured at $T = 100$ K for the $Co_3Sn_2S_2$ Hall-bar devices with $W = 1.0$ (top), 0.6, 0.4, and 0.2 μm (bottom).

tesla regardless of the growth technique and substrate materials [30,31,34], which suggests that the underlying mechanism of the magnetization switching in the thin films is fundamentally different from that of the bulk single crystals. The large H_c is a great benefit for the DW devices based on thin films with PMA because of the robust magnetization direction against external disturbance. Thus, the understanding of the mechanism of magnetization switching is inevitable for the thermally stable operation of DW devices.

In thin-film devices with a large PMA, the magnetization switching is generally governed by three possible mechanisms depending on the size and the shape: (i) the coherent or incoherent rotation without DW formation, (ii) sequential formation of the reversed domain nucleus, or (iii) expansion of the reversed magnetic domains with event overcoming pinning sites, i.e., the DW propagation to pinning sites. The thermal stability of a magnetic particle against the thermal agitation $k_B T$, with k_B and T being the Boltzmann constant and temperature, respectively, is evaluated by the energy E under the magnetic field H, which is given by [35]

$$E = E_0\left(1 - \frac{H}{H_0}\right)^2, \tag{1}$$

where

$$E_0 = \mu_0 H_0 M_s V. \tag{2}$$

Here, H_0, M_s, and V are an intrinsic coercivity, saturation magnetization, and volume of the particle, respectively. When H reaches H_0, the E becomes zero and the magnetization switches without thermal activation. Below, we discuss the three magnetization switching mechanisms of the fully magnetized state along the perpendicular to the film plane. The rotation mode generally appears when the size of devices is smaller than the DW width, where the magnetization switches without DW formation because the energy cost to form DW is larger than the effective magnetic anisotropy energy. In this mode, the E_0 is given by $\mu_0 H_0 M_s V = 2K_{eff}V$, with K_{eff} being an effective magnetic anisotropy energy. Thus, the magnetization switching through the coherent rotation occurs at $\mu_0 H_c = \mu_0 H_0 = 2K_{eff}/M_s = \mu_0 H_A$. When the device size is larger than the DW width, H_c is characterized by the nucleation field (H_n) required to introduce the reversed domain nucleus with its volume V_n and diameter of d_n, and/or by the depinning field (H_p) for the propagating DW [36,37]. When H_p is larger than H_n at all of the nucleation sites, nucleation occurs at randomly distributed local defect sites, resulting in the H_0 becoming the nucleation field $H_n(< H_A)$. In this case, magnetization in the whole area of the device switches by

sequential switching of the small reversed domain nuclei at different sites and H_c is characterized by the average value of H_n. On the other hand, when the H_p is larger than the smallest H_n among the nucleation sites, the reversed domain nucleus is formed at the weakest nucleation site with the smallest E_0, and then the DW instantly propagates to the pinning site with H_p, resulting in the formation of the reversed magnetic domain with its diameter $d > d_n$. The other nucleation sites with larger H_n than H_p do not participate in the magnetization switching in the area of d. In this case, the value of d should be an inverse function of the density of the DW pinning sites. The magnetization switching process has been investigated by means of Lorentz microscope, magnetic force microscope, and magneto-optic Kerr effect microscope [38–40], scanning superconducting quantum interference device [41], and Hall-effect magnetometry [42,43]. Among them, the Hall effect magnetometry using AHE [44] is a simple technique with a microstructured device, being sensitive to the local variation of perpendicular magnetization of the ferromagnetic thin films and applicable in a wide range of temperature. To elucidate the microscopic mechanism of the magnetization switching in the $Co_3Sn_2S_2$ thin film, the Hall-effect measurement in the submicrometer-wide constricted devices is an effective approach in particular for detecting the submicrometer-size domains as it enables the observation of local variation of magnetic domain and DW through the large AHE.

In this study, we measured the longitudinal (R_{xx}) and Hall (R_{yx}) resistances upon changing the magnetic field (H) in submicrometer-wide wire devices based on the $Co_3Sn_2S_2$ thin film with a thickness $t = 40$ nm to explore the mechanism of magnetization switching. In the wire devices with a width of below 0.6 μm, the discretized profiles emerge in the hysteresis loops of R_{yx}, which detect the local magnetization switching events accompanied with the formation of the reversed domain nuclei and/or the DW propagation. By counting the number of individual switching events in $R_{yx}(H)$, the reversed magnetic domain diameter d is estimated to be about 80 nm, which is much smaller than the bulk value of a few to hundreds of micrometers [28,29]. In contrast, the diameter of the reversed domain nucleus d_n and the intrinsic nucleation field $\mu_0 H_n$ are estimated to be 2.4 nm and 8.0 T, respectively, by considering the energy barrier $E_0 = \mu_0 H_n M_s V_n = \mu_0 H_n M_s \pi t (\frac{d_n}{2})^2$ required for formation of the reversed domain nucleus [45]. Our findings suggest that the large H_n and strong pinning of the DW of the reversed magnetic domain play a dominant role in the larger H_c of the $Co_3Sn_2S_2$ thin films than that of bulk crystals.

II. EXPERIMENTAL DETAILS

The $Co_3Sn_2S_2$ submicrometer-wide wire devices were fabricated from a single film of SiO_x cap/40 nm $Co_3Sn_2S_2$ on an Al_2O_3 (0001) substrate grown by radio-frequency sputtering [30,46]. Thickness of the $Co_3Sn_2S_2$ thin film was determined by the thickness fringes of x-ray diffraction pattern around $Co_3Sn_2S_2$ (0006) (see Supplemental Material, Fig. S1 [46]). By using electron-beam lithography and Ar ion milling, the widths W and length L of the wire devices were designed to $W = 1.0$, 0.6, 0.4, and 0.2 μm and $L = 3W$, as shown

in Fig. 1(b). Electrical measurements were carried out by standard lock-in technique with a modulation frequency of 13 Hz in a physical properties measurements system (Quantum Design) equipped with a 9-T superconducting magnet. A schematic of the $Co_3Sn_2S_2$ wire device is shown in Fig. 1(c), which illustrates the local formation of reversed magnetic domains with magnetizations directed downward when the external perpendicular magnetic field H is swept from a positive saturation field to a negative value. The ensemble average of the magnetic domains around the Hall probe with an area of W^2 can be detected as the AHE signal.

III. RESULTS AND DISCUSSION

Figures 1(d) and 1(e) show the temperature T dependence of the R_{xx} and R_{yx} of the wire devices measured under $\mu_0 H = 0$ T after field cooling at 1 T. The kink feature was observed in R_{xx} at 180 K, which reflects the T_C. The values of R_{yx} below the T_C are not apparently different between all the wire devices, and the anomalous Hall resistivity of the devices is comparable to that of bulk crystals [5], indicating that the lithography process induces negligibly small damages to the electrical transport and magnetic properties. Figures 1(f) and 1(g) show $\mu_0 H$ dependence of R_{xx} and R_{yx}, respectively, at $T = 100$ K for the wire devices with $W = 1.0$ (top panel), 0.6, 0.4, and 0.2 μm (bottom panel). Clear butterfly-shaped hysteresis in $R_{xx}(H)$ and polarity change in $R_{yx}(H)$ were observed at comparable magnetic field for all the devices, which we defined as the coercivity H_c. The asymmetric features and negative magnetoresistance in $R_{xx}(H)$ may come from superposition of the nonzero transverse resistance contribution due to the alignment offset of the voltage probes. The peak amplitude of the $R_{xx}(H)$ becomes more pronounced in the narrower devices from about 2% of $R_{xx}(H = 0)$ for $W = 1.0$ μm to about 5% for $W = 0.2$ μm. Although the butterfly-shaped MR has rarely been discussed in the bulk $Co_3Sn_2S_2$, the prominent butterfly hysteresis in the constricted device suggests the increased contribution of DWs to $R_{xx}(H)$, which has been discussed in thin-film devices of typical ferromagnetic materials [47–49]. The $R_{yx}(H)$ values for the wire devices with $W = 0.6$, 0.4, and 0.2 μm exhibit stepwise profiles in contrast to the rather smooth variation of $R_{yx}(H)$ for $W = 1.0$ μm [top panel in Fig. 1(g)]. The discretized step becomes more remarkable for the smaller W, indicating that the R_{yx} detects the subsequent formation of the reversed magnetic domain and/or depinning of the DWs in the constricted geometry.

To estimate the size of the reversed magnetic domains d formed in the wire devices from the discontinuous changes in R_{yx} in the H variation, the $R_{yx}(H)$ measured on decreasing H is differentiated. Figure 2(a) shows the $\mu_0 H$ dependence of $d(R_{yx}/R_{yx}^0)/d(\mu_0 H)$ and R_{yx}/R_{yx}^0 (inset) for $W = 0.2$ μm at $T = 40$ K on decreasing H. Here, R_{yx}/R_{yx}^0 stands for the Hall resistance normalized by the remanent R_{yx} at $\mu_0 H = 0$ T. The spike features denoted with black small lines in $d(R_{yx}/R_{yx}^0)/d(\mu_0 H)$ correspond to the steps in the discretized R_{yx}/R_{yx}^0 (see inset). The identical plots in the magnified magnetic field range around magnetization reversal are shown in Supplemental Material, Fig. S2 [46]. For example, individual
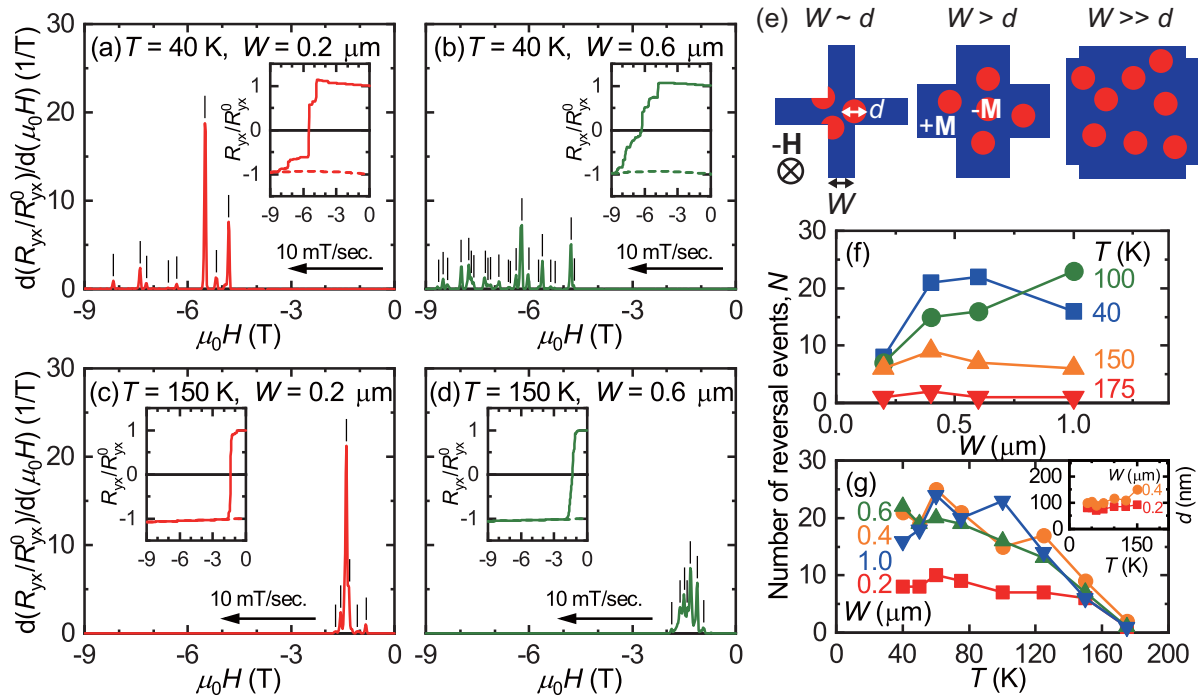
FIG. 2. (a), (b) Normalized Hall resistance differentiated with the magnetic field $d(R_{yx}/R_{yx}^0)/d(\mu_0 H)$ vs $\mu_0 H$ data at $T = 40$ K for the Co$_3$Sn$_2$S$_2$ wire devices with $W =$ (a) 0.2 μm and (b) 0.6 μm. Insets show the corresponding R_{yx}/R_{yx}^0 vs $\mu_0 H$ data. (c), (d) Same dataset with (a) and (b) measured at $T = 150$ K for the Co$_3$Sn$_2$S$_2$ wire devices with $W =$ (c) 0.2 μm and (d) 0.6 μm. (e) Schematics of the reversed magnetic domain with its diameter d in the Co$_3$Sn$_2$S$_2$ wire devices with the channel width W. Red and blue areas represent the magnetic domain with the magnetization oriented parallel and antiparallel to $\mu_0 H$, respectively. (f), (g) Number of switching events as a function of (f) W and (g) T. Inset in (g) shows estimated d value as a function of T for $W = 0.2$ μm.

eight spikes can be counted in Fig. 2(a), meaning that the reversed magnetic domains with their diameter d are generated eight times in the Hall-probe area. The same set of $d(R_{yx}/R_{yx}^0)/d(\mu_0 H)$ for the device with $W = 0.6$ μm is shown in Fig. 2(b). The spike features are more frequently observed, indicating the increased number of local magnetization switching events in the wide area W^2. In this consideration, we assume that the size of d is independent of W [45]. Although the stepwise $R_{yx}(H)$ is less significant at high temperature $T = 150$ K as shown in Figs. 2(c) and 2(d), the reduction of spike features in $d(R_{yx}/R_{yx}^0)/d(\mu_0 H)$ indicates that multiple switching events simultaneously occur in various areas at small H.

Figure 2(e) illustrates a possible scenario for the magnetization switching process in the active area W^2 in the wire devices, based on the formation of the reversed magnetic domain with d. When d is comparable to W, local variation of the magnetization is dominant in the variation of $R_{yx}(H)$. The number of the steps observed in $R_{yx}(H)$ is regarded as the number of local magnetization switching events N. When we assume a constant nucleation density, N increases quadratically with the size of the Hall cross ($N =$ density $\times W^2$). However, as the spike feature in $d(R_{yx}/R_{yx}^0)/d(\mu_0 H)$ has the infinite peak width (ΔH) along the magnetic field, there is an upper limit of the number of countable switching events. Here, we define ΔH as the full width at half maximum of the spike features in $d(R_{yx}/R_{yx}^0)/d(\mu_0 H)$, which ranges from 40 to 100 mT (see Supplemental Material, Fig. S3 [46]). Multiple generations of the reversed magnetic domains frequently occur in large active areas, which are inevitably counted as a single event of magnetization switching, leading to the saturation of the nominal N characterized by ΔH at the large W. At the condition of W much larger than d, the electrical detection of the magnetic switching events by Hall probe is unavailable because $R_{yx}(H)$ behaves like a smooth transition due to small variation of R_{yx} at the individual switching events. As shown in Fig. 2(f), we obtain the saturation behavior in $W \geqslant 0.6$ μm at $T = 40$ K and 100 K. In the following, we employed N at $W = 0.2$ and 0.4 μm for estimation of d, where the separation between the neighboring spike features in $d(R_{yx}/R_{yx}^0)/d(\mu_0 H)$ is wide enough to assign each spike as formation of a single reversed magnetic domain. Note that the 40 K is the lowest temperature, at which we were able to fully switch the magnetization of the Co$_3$Sn$_2$S$_2$ device using the magnet of our apparatus. The increase of N with W from $W = 0.2$ to 0.4 μm suggests that individual magnetization switching events occur at defect sites in the device rather than edges of the device. Such a W dependence of N was not observed at $T = 150$ and 175 K because thermal activation may support the nucleation and/or DW propagation occurring at a low magnetic field, resulting in sharp magnetization switching around H_c for $W = 0.2$ [Fig. 2(c)] and 0.6 μm [Fig. 2(d)]. Figure 2(g) shows T dependence of N for different W. The values of N for $W = 0.4$, 0.6, and 1.0 μm show the saturation behavior below $T = 100$ K. Interestingly, the N for the wire device with $W = 0.2$ μm is almost independent of T below
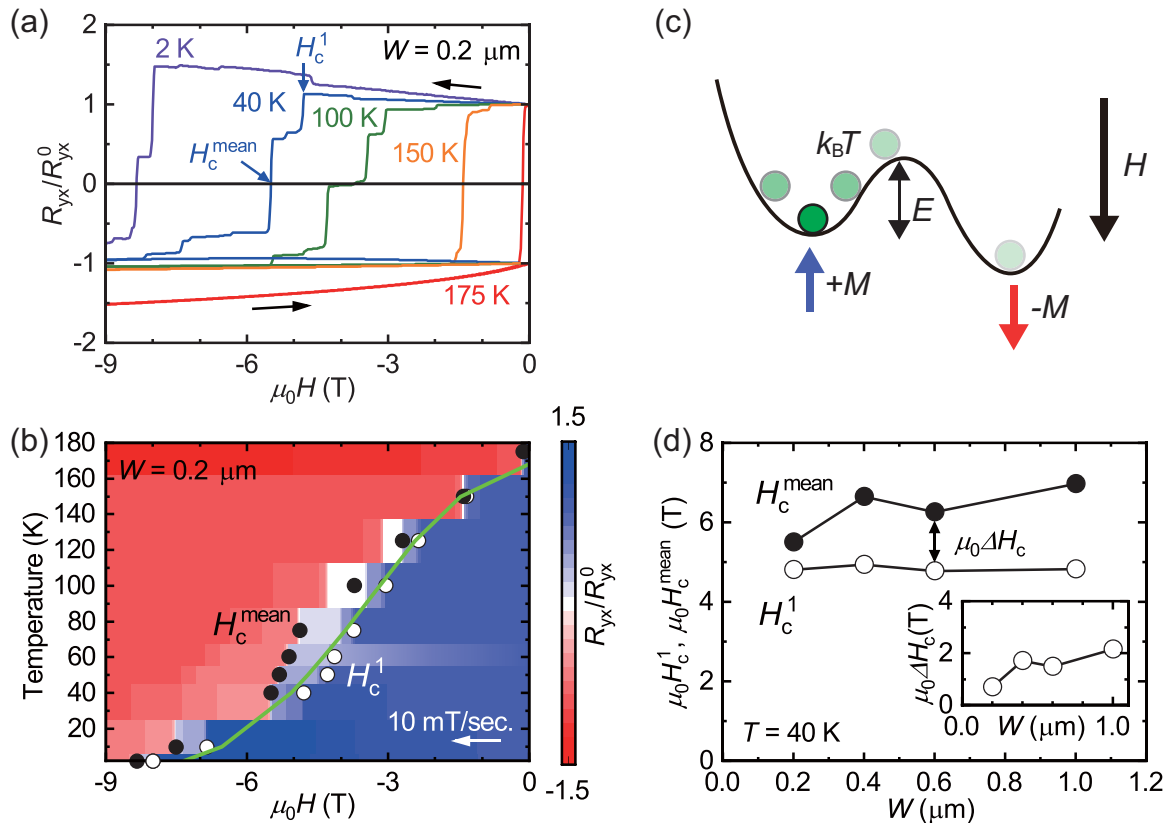
FIG. 3. (a) Magnetic field dependence of the normalized Hall resistance R_{yx}/R_{yx}^0 at $T = 2$ (purple), 40 (blue), 100 (green), 150 (orange), and 175 K (red) for the 0.2-μm-wide $Co_3Sn_2S_2$ device. Black solid arrows indicate a sweep direction. (b) Contour plot of R_{yx}/R_{yx}^0 as a function of T and μ_0H. The critical field H_c^1 and the coercivity H_c^{mean} denote the magnetic field when the first nucleation event occurs and when the R_{yx} becomes zero, respectively. A green solid line denotes a fitting curve based on Eq. (3). (c) Schematic of thermal activation and magnetization switching under the external magnetic field H. (d) Wire width W dependences of H_c^1 and H_c^{mean} at $T = 40$ K. Inset shows the magnetic field difference $\Delta H_c = H_c^{mean} - H_c^1$.

150 K, reflecting no T variation of the density of nucleation sites possessing H_n smaller than H_p [50]. This fact may imply that the magnetization switching events occur at the same nucleation sites with the weakest magnetic anisotropy, although all the measurements were performed after fully magnetized process. Note that if the magnetization switching is governed by the sweeping of the single DW, the value of N corresponds to the number of pinning sites with the pinning energy larger than k_BT and should decrease with increasing T. The value of d calculated by N assuming cylindrical reversed magnetic domain in the device with $W = 0.2$ μm using the relation $W^2/N = \pi(d/2)^2$ was about 80 nm, which is independent of T up to $T = 150$ K (see inset in Fig. 2(g)). This value is comparable to the 90 nm in the 0.4 μm device, which is consistent with the monotonic increase behavior in Fig. 2(f). In contrast, the d for the device with $W = 0.6$ and 1.0 μm is roughly estimated to be 140 and 280 nm, respectively. These large values of d reflect the area ratio of the reversed magnetic domains and W^2, indicating that a nominally individual magnetic switching event consists of simultaneous formation of the multiple reversed magnetic domains with the certain density. Our simple model, which introduces the cylindrical domain representing the averaged area increase of the reversed magnetic domain, is applicable for both subsequential formation of the magnetic domain nuclei and DW expansion,

and a single DW propagation across the active area of the Hall device.

Figure 3(a) shows the μ_0H dependences of R_{yx}/R_{yx}^0 for the wire device with $W = 0.2$ μm at $T = 2, 40, 100, 150$, and 175 K. We define the critical field H_c^1 and a coercivity H_c^{mean}, where the first switching event occurs and the R_{yx} becomes zero, respectively, on decreasing H from a positive saturation field. Although complete magnetization switching is not achieved in our apparatus at $T = 2$ K, the H_c^1 and H_c^{mean} can be obtained by the measurement from the positive saturation condition after field cooling. At $T = 40$ K, the switching events sharply occur at each step of $R_{yx}(H)$ in a wide range of magnetic field from H_c^1 of about -5 T to saturation field of around -8 T. These sharp steps are indicative of formation of the reversed magnetic domain at nucleation sites with the largely different H_n. The reversed magnetic domains do not enlarge progressively due to the strong pinning sites. The H_c^1 of about -1 T at 150 K is much larger than that of the bulk crystals, which reflects the specific mechanism of the nucleation and DW pinning in thin films. Figure 3(b) illustrates temperature evolution of H_c^1 and H_c^{mean}, both of which increase with decreasing T, indicating that magnetization switching takes place through the thermal activation mechanism [Fig. 3(c)]. At $H = H_c^1$, the reversed domain nucleus is formed at the site with the lowest energy

barrier. Under the continuous sweeping of the external magnetic field, H_c^1 in the nucleation-type mechanism is given by the following equation [51]:

$$H_c^1 = H_n \left\{ 1 - \left[\frac{k_B T}{E_0} \ln \left(\frac{f_0 \tau}{\ln 2} \right)^{1/2} \right] \right\}, \qquad (3)$$

where f_0 is the attempt frequency (assumed to be 1×10^9 Hz). The elapsed time τ to reach H_c^1 was calculated by the sweep rate of 10 mT/s. The H_n is an intrinsic nucleation field at zero temperature and $E_0 = \mu_0 H_n M_s V_n$. Temperature dependence of H_c^1 is well fitted based on Eq. (3) using H_n and V_n as free parameters, providing that $\mu_0 H_n = 8.0$ T and $V_n = 1.8 \times 10^2$ nm³ [green solid line in Fig. 3(b)]. The value of $\mu_0 H_n$ is smaller than $\mu_0 H_A$ of the thin films (18 T at 100 K [34]), which is consistent with the nucleation-type mechanism [either (ii) or (iii)]. The thermal stability $E_0/k_B T$ of the reversed domain nucleus for the wire device with $W = 0.2$ μm was obtained as 200 at $T = 40$ K and 20 at 175 K. The rather high thermal stability in the vicinity of T_C is consistent with the high PMA character of $Co_3Sn_2S_2$ with the superior remanent magnetization remaining even at high temperature [34]. Assuming a cylindrical shape for the reversed domain nucleus [$d_n = 2(V_n/t\pi)^{1/2}$], its diameter d_n was calculated to be 2.4 nm, which was only 3% of d determined in Fig. 2 and comparable to the domain-wall width, which is estimated as a few nanometers in the $Co_3Sn_2S_2$ bulk crystal by neutron-scattering experiments [28]. Considering the much smaller value of d_n than the diameter of the reversed magnetic domain d for the wire device with $W = 0.2$ μm, the DW propagation mechanism is likely to be dominant in the device [mechanism (iii)]. The device size dependence of H_c^1 remains almost constant at roughly 5 T at $T = 40$ K [Fig. 3(d)], which supports our assumption that H_c^1 corresponds to H_n. No size dependence of H_c^1 reflects the intrinsic origin in the magnetization switching process in the $Co_3Sn_2S_2$ film. If concomitant formation of the multiple small reversed domain nuclei [mechanism (ii)] plays a role, the W dependence of nominal N may not be detected in the investigated range of the W as the area ratio of the sum of multiple reversed magnetic nuclei and W^2 should be constant.

The estimated d and d_n of the $Co_3Sn_2S_2$ wire device with $W = 0.2$ μm at $T = 40$ K are plotted in Fig. 4. These values of the $Co_3Sn_2S_2$ wire device are compared with those of pillar-shaped devices with typical PMA ferromagnetic metal [37,45,52,53] and oxide (La,Sr)MnO₃ thin films [54] at room temperature, and magnetic semiconductor (Ga,Mn)As thin-film device at $T = 80$ K [55]. The values of d in CoFeB and CoPd are nearly the same as the d_n, suggesting that the DW propagation is suppressed by a strong DW pinning. In contrast, the value of d for (Ga,Mn)As is two orders of magnitude larger than d_n. It has been reported that the DW propagates through the energy-barrier landscape of the randomly distributed pinning sites [56,57]. In the $Co_3Sn_2S_2$ bulk single crystal, the reversed magnetic domains with a diameter of a few to hundreds of micrometers are reported [28,29], which is much larger than reversed domain nucleus ($V_n \sim 2.5 \times 10^5$ nm³ if estimated from an energy barrier for domain nucleation $E_0/k_B = 3000$ K). This fact is consistent with the DW propagation mechanism. The fact that the d
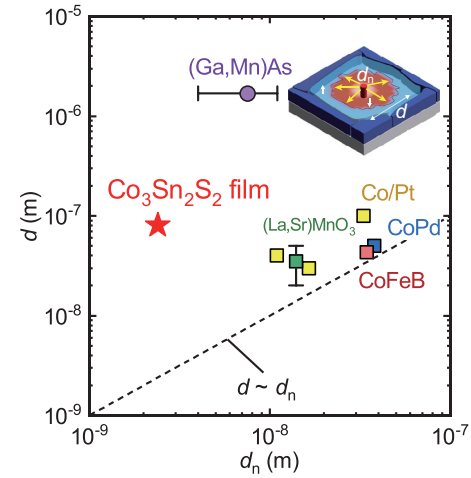

FIG. 4. Estimated diameters of the reversed magnetic domain vs those of the reversed domain nucleus in the $Co_3Sn_2S_2$ wire devices (red star) compared with a variety of magnetic thin films including perpendicular magnetized (Ga,Mn)As (purple) [55], Co/Pt multilayer and alloy (yellow) [45,53], CoPd alloy (blue) [37], and CoFeB (red square) [52], and in-plane magnetized (La,Sr)MnO₃ (green) [54]. Inset shows a schematic of the magnetic domain evolution after the formation of the reversed magnetic nucleus in a single-crystalline grain.

value of the $Co_3Sn_2S_2$ wire devices is one or two orders of magnitude larger than d_n points out that the magnetization switching is governed by the DW propagation [mechanism (iii)]. However, $d \sim 80$ nm in the wire devices is more than two orders of magnitude smaller than bulk value, which recalls the specific nucleation and pinning mechanism in thin films.

Finally, we discuss possible origins of the large nucleation field and strong pinning in the $Co_3Sn_2S_2$ device. In the mechanism (iii), the reversed domain nucleus is formed at the weakest nucleation site possessing the smallest H_n, and the DW propagates within the area of d as schematically shown in the inset of Fig. 4. The nucleation field H_n is strongly reduced from H_A if a point defect of the crystallinity or inhomogeneity of M_s is present. According to the analysis based on Eq. (3), the intrinsic H_n in the wire devices remains to be as large as 8.0 T, which is reduced by only about half of H_A. The large H_n suggests the relatively homogeneous crystallinity of the $Co_3Sn_2S_2$ thin film within the area characterized by d. The reversed magnetic domain with its diameter d is characterized by the DW pinning. The pinning sites may be the random point defects, crystal grain boundaries, or epitaxial strain inherent in thin films. Judging from the value of d being comparable to the size of crystalline grain (~ 10 nm in diameter) reported in the very thin-film (~ 2.7 nm in thickness) condition [33], the boundaries of slightly misoriented crystalline grains and thus, crystalline PMA, may be one of the feasible sources of pinning sites. In contrast, the bulk single crystal exhibits $\mu_0 H_c \sim 0.3$ T with a sharp switching [5,24], probably because the reversed domain nuclei emerge at point defects and the DWs instantly propagate through the whole single-crystalline sample. Concomitant realization of the large nucleation field H_n and depinning field H_p in

$Co_3Sn_2S_2$ thin films may be a scenario for explaining the enhanced coercivity. A large H_c is a great benefit for the DW devices aiming at current-induced phenomena as it makes the magnetization and the DWs to be robust against thermal agitation and Oersted field inherent to the electric current. Enlargement of reversed magnetic domain is preferable for observing and understanding of physical properties of the well-regulated single DW. The crystalline grains and thus, the reversed magnetic domain, may be further enlarged while maintaining uniform crystallinity, which would lead to observation of the exotic physical properties emerging at the single DW of $Co_3Sn_2S_2$ films.

IV. SUMMARY

In summary, the mechanism of the large H_c in the $Co_3Sn_2S_2$ thin film was investigated by evaluating the nucleation field and diameters of the reversed magnetic domain and comparing reversed domain nucleus in the $Co_3Sn_2S_2$ constricted wire devices. From discretized $R_{yx}(H)$ in the wire device with $W = 0.2$ μm, the reversed magnetic domain size is estimated to be 80 nm, which is one or two orders of magnitude larger than the reversed domain nucleus and much smaller than that reported in bulk single crystal. Our finding is suggestive evidence that the large H_c in thin-film form is dominated by the large nucleation field and strong pinning of the DW propagation. Concomitant realization of the large magnetic domain and the large H_c can be anticipated by engineering grain boundary, which would enable the observation of intriguing phenomena occurring at a single DW in the $Co_3Sn_2S_2$ thin-film devices.

[1] B. Yan and C. Felser, Topological materials: Weyl semimetals, Annu. Rev. Condens. Matter Phys. **8**, 337 (2017).

[2] N. P. Armitage, E. J. Mele, and A. Vishwanath, Weyl and Dirac semimetals in three-dimensional solids, Rev. Mod. Phys. **90**, 015001 (2018).

[3] C. Middleton, Magnetic semimetals host massless quasiparticles, Phys. Today **72** (12), 24 (2019).

[4] L. Ye, M. Kang, J. Liu, F. von Cube, C. R. Wicker, T. Suzuki, C. Jozwiak, A. Bostwick, E. Rotenberg, D. C. Bell, L. Fu, R. Comin, and J. G. Checkelsky, Giant anomalous Hall effect in a ferromagnetic Kagome-lattice semimetal, Nature (London) **555**, 638 (2018).

[5] E. Liu, Y. Sun, N. Kumar, L. Muechler, A. Sun, L. Jiao, S. Yang, D. Liu, A. Liang, Q. Xu et al., Giant anomalous Hall effect in a ferromagnetic kagome-lattice semimetal, Nat. Phys. **14**, 1125 (2018).

[6] Q. Wang, Y. Xu, R. Lou, Z. Liu, M. Li, Y. Huang, D. Shen, H. Weng, S. Wang, and H. Lei, Large intrinsic anomalous Hall effect in half-metallic ferromagnet $Co_3Sn_2S_2$ with magnetic Weyl fermion, Nat. Commun. **9**, 3681 (2018).

[7] S. Nakatsuji, N. Kiyohara, and T. Higo, Large anomalous Hall effect in a non-collinear antiferromagnet at room temperature, Nature (London) **527**, 212 (2015).

[8] M. Ikhlas, T. Tomita, T. Koretsune, M. Suzuki, D. Nishio-Hamane, R. Arita, Y. Otani, and S. Nakatsuji, Large anomalous Nernst effect at room temperature in a chiral antiferromagnet, Nat. Phys. **13**, 1085 (2017).

[9] A. Sakai, Y. P. Mizuta, A. A. Nugroho, R. Sihombing, T. Koretsune, M. Suzuki, N. Takemori, R. Ishii, D. Nishio-Hamane, R. Arita et al., Giant anomalous Nernst effect and quantum-critical scaling in a ferromagnetic semimetal, Nat. Phys. **14**, 1119 (2018).

[10] S. N. Guin, P. Vir, Y. Zhang, N. Kumar, S. J. Watzman, C. Fu, E. Liu, K. Manna, W. Schnelle, J. Gooth et al., Zero-field Nernst effect in a ferromagnetic Kagome-lattice Weyl-semimetal $Co_3Sn_2S_2$, Adv. Mater. **31**, 1806622 (2019).

[11] S. N. Guin, K. Manna, J. Noky, S. J. Watzman, C. Fu, N. Kumar, W. Schnelle, C. Shekhar, Y. Sun, J. Gooth et al., Anomalous Nernst effect beyond the magnetization scaling relation in the ferromagnetic Heusler compound Co_2MnGa, NPG Asia Mater. **11**, 16 (2019).

[12] H. Yang, W. You, J. Wang, J. Huang, C. Xi, X. Xu, C. Cao, M. Tian, Z.-A. Xu, J. Dai, and Y. Li, Giant anomalous Nernst effect in the magnetic Weyl semimetal $Co_3Sn_2S_2$, Phys. Rev. Mater. **4**, 024202 (2020).

[13] K. Sumida, Y. Sakuraba, K. Masuda, T. Kono, M. Kakoki, K. Goto, W. Zhou, K. Miyamoto, Y. Miura, T. Okuda et al., Spin-polarized Weyl cones and giant anomalous Nernst effect in ferromagnetic Heusler films, Commun. Mater. **1**, 89 (2020).

[14] T. Chen, S. Minami, A. Sakai, Y. Wang, Z. Feng, T. Nomoto, M. Hirayama, R. Ishii, T. Koretsune, R. Arita et al., Large anomalous Nernst effect and nodal plane in an iron-based kagome ferromagnet, Sci. Adv. **8**, eabk1480 (2022).

[15] N. Nagaosa, T. Morimoto, and Y. Tokura, Transport, magnetic and optical properties of Weyl materials, Nat. Rev. Mater. **5**, 621 (2020).

[16] Y. Okamura, S. Minami, Y. Kato, Y. Fujishiro, Y. Kaneko, J. Ikeda, J. Muramoto, R. Kaneko, K. Ueda, V. Kocsis et al., Giant magneto-optical responses in magnetic Weyl semimetal $Co_3Sn_2S_2$, Nat. Commun. **11**, 4619 (2020).

[17] L. Muechler, E. Liu, J. Gayles, Q. Xu, C. Felser, and Y. Sun, Emerging chiral edge states from the confinement of a magnetic Weyl semimetal in $Co_3Sn_2S_2$, Phys. Rev. B **101**, 115106 (2020).

[18] Y. Araki, A. Yoshida, and K. Nomura, Universal charge and current on magnetic domain walls in Weyl semimetals, Phys. Rev. B **94**, 115312 (2016).

[19] Y. Araki and K. Nomura, Charge Pumping Induced by Magnetic Texture Dynamics in Weyl Semimetals, Phys. Rev. Appl. **10**, 014007 (2018).

[20] K. Kobayashi, Y. Ominato, and K. Nomura, Helicity-protected domain-wall magnetoresistance in ferromagnetic Weyl semimetal, J. Phys. Soc. Jpn. **87**, 073707 (2018).

[21] D. Kurebayashi and K. Nomura, Theory for spin torque in Weyl semimetal with magnetic texture, Sci. Rep. **9**, 5365 (2019).

[22] S. Natarajan, G. V. Subba Rao, R. Baskaran, and T. S. Radhakrishnan, Synthesis and electrical properties of shandite-parkerite phases, A_2M_3Ch, J. Less-Common Met. **138**, 215 (1988).

[23] W. Schnelle, A. Leithe-Jasper, H. Rosner, F. M. Schappacher, R. Pöttgen, F. Pielnhofer, and R. Weihrich, Ferromagnetic ordering and half-metallic state of $Sn_2Co_3S_2$ with the shandite-type structure, Phys. Rev. B **88**, 144404 (2013).

[24] M. A. Kassem, Y. Tabata, T. Waki, and H. Nakamura, Quasi-two-dimensional magnetism in Co-based shandites, J. Phys. Soc. Jpn. **85**, 064706 (2016).

[25] N. Morali, R. Batabyal, P. K. Nag, E. Liu, Q. Xu, Y. Sun, B. Yan, C. Felser, N. Avraham, and H. Beidenkopf, Fermi-arc diversity on surface terminations of the magnetic Weyl semimetal $Co_3Sn_2S_2$, Science **365**, 1286 (2019).

[26] D. F. Liu, A. J. Liang, E. K. Liu, Y. W. Li, C. Chen, D. Pei, W. J. Shi, S. K. Mo, P. Dudin, T. Kim *et al.*, Magnetic Weyl semimetal phase in a kagomé crystal, Science **365**, 1282 (2019).

[27] A. Sugawara, T. Akashi, M. A. Kassem, Y. Tabata, T. Waki, and H. Nakamura, Magnetic domain structure within half-metallic ferromagnetic kagome compound $Co_3Sn_2S_2$, Phys. Rev. Mater. **3**, 104421 (2019).

[28] C. Lee, P. Vir, K. Manna, C. Shekhar, J. E. Moore, M. A. Kastner, C. Felser, and J. Orenstein, Observation of a phase transition within the domain walls of ferromagnetic $Co_3Sn_2S_2$, Nat. Commun. **13**, 3000 (2022).

[29] Z. Shen, X. Zhu, R. R. Ullah, P. Klavins, and V. Taufour, The depinning of magnetic domain walls and the magnetization anomaly within the ferromagnetic phase of the Weyl semimetal $Co_3Sn_2S_2$, arXiv:2205.06420.

[30] K. Fujiwara, J. Ikeda, J. Shiogai, T. Seki, K. Takanashi, and A. Tsukazaki, Ferromagnetic $Co_3Sn_2S_2$ thin films fabricated by co-sputtering, Jpn. J. Appl. Phys. **58**, 050912 (2019).

[31] S. Li, G. Gu, E. Liu, P. Cheng, B. Feng, Y. Li, L. Chen, and K. Wu, Epitaxial growth and transport properties of magnetic Weyl semimetal $Co_3Sn_2S_2$ thin films, ACS Appl. Electron. Mater. **2**, 126 (2020).

[32] J. Ikeda, K. Fujiwara, J. Shiogai, T. Seki, K. Nomura, K. Takanashi, and A. Tsukazaki, Critical thickness for the emergence of Weyl features in $Co_3Sn_2S_2$ thin films, Commun. Mater. **2**, 18 (2021).

[33] J. Ikeda, K. Fujiwara, J. Shiogai, T. Seki, K. Nomura, K. Takanashi, and A. Tsukazaki, Two-dimensionality of metallic surface conduction in $Co_3Sn_2S_2$ thin films, Commun. Phys. **4**, 117 (2021).

[34] J. Shiogai, J. Ikeda, K. Fujiwara, T. Seki, K. Takanashi, and A. Tsukazaki, Robust perpendicular magnetic anisotropy of $Co_3Sn_2S_2$ phase in sulfur deficient sputtered thin films, Phys. Rev. Mater. **5**, 024403 (2021).

[35] E. C. Stoner and E. P. Wohlfarth, A mechanism of magnetic hysteresis in heterogeneous alloys, Philos. Trans. R. Soc. London, Ser. A **240**, 599 (1948).

[36] J. P. Jamet, S. Lemerle, P. Meyer, J. Ferré, B. Bartenlian, N. Bardou, C. Chappert, P. Veillet, F. Rousseaux, D. Decanini *et al.*, Dynamics of the magnetization reversal in Au/Co/Au micrometer-size dot arrays, Phys. Rev. B **57**, 14320 (1998).

[37] T. Thomson, G. Hu, and B. D. Terris, Intrinsic Distribution of Magnetic Anisotropy in Thin Films Probed by Patterned Nanostructures, Phys. Rev. Lett. **96**, 257204 (2006).

[38] J. Raabe, R. Pulwey, R. Sattler, T. Schweinböck, J. Zweck, and D. Weiss, J. Appl. Phys. **88**, 4437 (2000).

[39] T. Shinjo, T. Okuno, R. Hassdorf, K. Shigeto, and T. Ono, Science **289**, 930 (2000).

[40] A. Hubert and R. Schäfer, *Magnetic Domains—The Analysis of Magnetic Microstructures* (Springer, Berlin, 1998).

[41] W. Wernsdorfer, K. Hasselbach, D. Mailly, B. Barbara, A. Benoit, L. Thomas, and G. Suran, DC-SQUID magnetization measurements of single magnetic particles, J. Magn. Magn. Mater. **145**, 33 (1995).

[42] A. K. Geim, S. V. Dubonos, J. G. S. Lok, I. V. Grigorieva, J. C. Maan, L. T. Hansen, and P. E. Lindelof, Ballistic Hall micromagnetometry, Appl. Phys. Lett. **71**, 2379 (1997).

[43] M. Rahm, M. Schneider, J. Biberger, R. Pulwey, J. Zweck, D. Weiss, and V. Umansky, Vortex nucleation in submicrometer ferromagnetic disks, Appl. Phys. Lett. **82**, 4110 (2003).

[44] N. Kikuchi, R. Murillo, and J. C. Lodder, AHE measurements of very thin films and nanosized dots, J. Magn. Magn. Mater. **287**, 320 (2005).

[45] N. Kikuchi, K. Mitsuzuka, T. Shimatsu, O. Kitakami, and H. Aoi, Nucleation size of hcp-CoPt dot arrays characterized by time dependence of coercivity, J. Phys. Conf. Ser. **200**, 102003 (2010).

[46] See Supplemental Material at http://link.aps.org/supplemental/10.1103/PhysRevMaterials.6.114203 for the growth condition and structural characterization of the $Co_3Sn_2S_2$ thin films.

[47] A. P. Mihai, J. P. Attané, A. Marty, P. Warin, and Y. Samson, Electron-magnon diffusion and magnetization reversal detection in FePt thin films, Phys. Rev. B **77**, 060401(R) (2008).

[48] P. Li, L. T. Zhang, W. B. Mi, E. Y. Jiang, and H. L. Bai, Origin of the butterfly-shaped magnetoresistance in reactive sputtered epitaxial Fe_3O_4 films, J. Appl. Phys. **106**, 033908 (2009).

[49] D. Chiba, M. Yamanouchi, F. Matsukura, T. Dietl, and H. Ohno, Domain-Wall Resistance in Ferromagnetic (Ga,Mn)As, Phys. Rev. Lett. **96**, 096602 (2006).

[50] D. B. Gopman, D. Bedau, S. Mangin, E. E. Fullerton, J. A. Katine, and A. d. Kent, Temperature dependent nucleation, propagation, and annihilation of domain walls in all-perpendicular spin-valve nanopillars, J. Appl. Phys. **115**, 113910 (2014).

[51] P. Sharrock and J. T. McKinney, Kinetic effects in coercivity measurements, IEEE Trans. Magn. **MAG-17**, 3020 (1981).

[52] Y. Takeuchi, H. Sato, S. Fukami, F. Matsukura, and H. Ohno, Temperature dependence of energy barrier in CoFeB-MgO magnetic tunnel junctions with perpendicular easy axis, Appl. Phys. Lett. **107**, 152405 (2015).

[53] J. Moritz, B. Dienya, and J. P. Nozières, Magnetization dynamics and thermal stability in patterned media, Appl. Phys. Lett. **86**, 063512 (2005).

[54] R. Akiyama, H. Tanaka, T. Matsumoto, and T. Kawai, Spin-polarized scanning tunneling microscopy on half-metallic manganite thin film with half-metallic manganite tip, Appl. Phys. Lett. **79**, 4378 (2001).

[55] C. Gourdon, A. Dourlat, V. Jeudy, K. Khazen, H. J. von Bardeleben, L. Thevenard, and A. Lemaître,

Determination of the micromagnetic parameters in (Ga,Mn)As using domain theory, Phys. Rev. B **76**, 241301(R) (2007).

[56] L. Thevenard, L. Largeau, O. Mauguin, G. Patriarche, A. Lemaître, N. Vernier, and J. Ferréet, Magnetic properties and domain structure of (Ga,Mn)As films with perpendicular anisotropy, Phys. Rev. B **73**, 195331 (2006).

[57] M. Yamanouchi, J. Ieda, F. Matsukura, S. E. Barnes, S. Maekawa, and H. Ohno, Universality classes for domain wall motion in the ferromagnetic semiconductor (Ga,Mn)As, Science **317**, 1726 (2007).

[58] K. Momma and F. Izumi, *VESTA 3* for three-dimensional visualization of crystal, volumetric and morphology data, J. Appl. Crystallogr. **44**, 1272 (2011).